sciendo | Journal of Electrical Bioimpedance | JoEB bioimpedance.net

J Electr Bioimp, vol. 10, pp. 14-23, 2019
Received 28 Nov 2018 / published 1 Jul 2019
https://doi.org/10.2478/joeb-2019-0003

Dielectrical properties of living epidermis and dermis in the frequency range from 1 kHz to 1 MHz

B. Tsai[1], H. Xue[1], E. Birgersson[2], S. Ollmar[3] and U. Birgersson[3,4]

1. *Department of Chemical and Biomolecular Engineering, National University of Singapore, 4 Engineering Drive 4, Singapore 117585*
2. *Department of Mechanical Engineering, National University of Singapore, 5 Engineering Drive 2, Singapore 117576*
3. *Department of Clinical Science, Intervention and Technology, Karolinska Institutet, SE-14186 Stockholm Sweden*
4. *E-mail any correspondence to: ulrik.birgersson@ki.se*

Abstract

We determine the in-vivo dielectric properties—resistivity and relative permittivity—of living epidermis and dermis of human skin soaked with a physiological saline solution for one minute between 1 kHz and 1 MHz. This is done by fitting approximate analytical solutions of a mechanistic model for the transport of charges in these layers to a training set comprising impedance measurements at two depth settings on stripped skin on the volar forearm of 24 young subjects. Here, the depth settings are obtained by varying the voltage at a second inject on the electrical-impedance-spectroscopy probe. The model and the dielectric properties are validated with a test set for a third depth setting with overall good agreement. In addition, the means and standard deviations of the thicknesses of living epidermis and dermis are estimated from a literature review as 61±7 µm and 1.0±0.2 mm respectively. Furthermore, extensions to resolve the skin layers in more detail are suggested.

Keywords: Dermis, epidermis, electrical impedance spectroscopy, in-vivo, relative permittivity, resistivity, skin thickness

Introduction

The human skin comprises several layers—stratum corneum (SC), living epidermis (LE), dermis (DE) and hypodermis—with different dielectric properties that are functions of not only the frequency of the applied voltage but also other factors such as age [1] and health condition [2] during electrical impedance spectroscopy (EIS) measurements.

The dielectric properties of human skin have been studied experimentally for different locations and frequencies. A database treating the skin as a one-layer entity for both wet and dry skin has been compiled for in-vivo EIS measurements in the frequency range 100 Hz to 20 GHz [3]. A higher resolution of the inherent layers was achieved through tape-stripping and in-vivo EIS, which established the dielectric properties of stratum corneum from 1 kHz to 1 MHz [4-6] and viable skin with living epidermis and dermis lumped together from 1 kHz to 1 MHz [5,6]. In addition, in-vitro EIS measurements of epidermis and devitalized dermis in a nutrient liquid saturation was carried out from 1 Hz to 100 kHz [7,8].

In view of the lack of in-vivo dielectric properties in the living epidermis and dermis between 1 kHz and 1 MHz, we apply and extend our old methodology of fitting a mechanistic mathematical model to experimental EIS measurements [6,9]. In essence, the methodology was applied to determine the dielectric properties of viable skin (living epidermis and dermis combined into one layer) and stratum corneum from two separate measurement series of stripped and intact skin respectively. The advantage of the mechanistic model is that it captures the local transport of charges throughout the skin layers and the EIS probe (see Fig. 1a-b); its main disadvantage, however, is the significant computational overhead since a complex-valued partial differential equation (PDE) needs to be solved numerically in several domains. We have recently managed to secure approximate analytical solutions [10,11] that reduce the multidomain PDE to a set comprising improper integrals and closed-form equations. This reduction is key when we here fit the dielectric properties of both living epidermis and dermis at the same time, because it becomes significantly more computationally difficult to fit four parameters at once—as compared to fitting only two for viable skin [9].

Besides introducing the approximate analytical solutions, we also tap into more information from the EIS measurements of stripped skin: the different charge pathways underneath the four-electrode, two-point-measurement EIS probe for the depth settings, which were obtained by varying the voltage at the second inject (see Fig. 1). A total of five depth settings are employed, out of which we choose depth settings 1 and 5 as the training set for parameter fitting and depth setting 3 as the test set for validation.

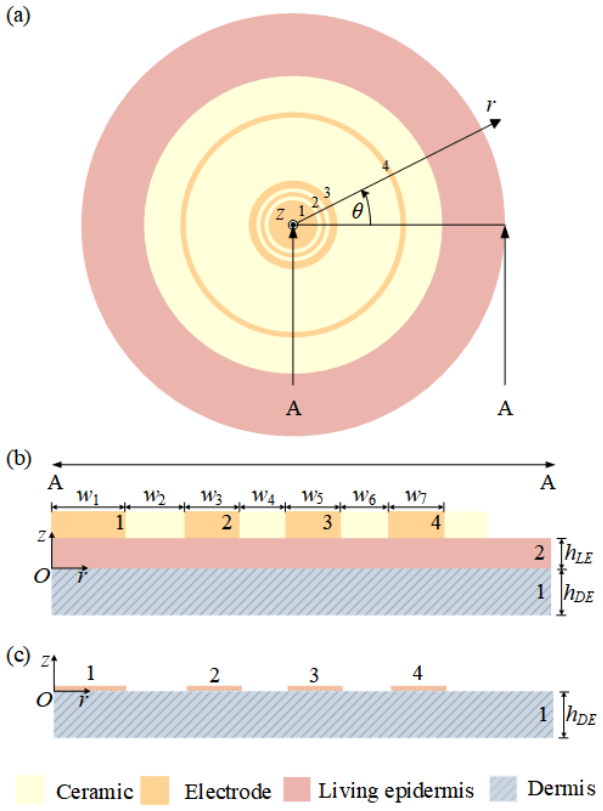

Fig.1: Schematic of (a) the four-electrode EIS probe with a sense (1), guard (2), second inject (3) and first inject (4); (b) the electrodes of the probe and the stripped skin comprising living epidermis and dermis; and (c) the reduced model consisting of dermis with the living epidermis and electrodes reduced to boundary conditions.

The layout of the paper is as follows: First, we summarize the experiments from our earlier study [9] and estimate the thicknesses of living epidermis and dermis from a literature survey. We then work through the main steps in the derivation towards the approximate analytical solution, which combines the idea of model reduction [10] and the generic, multi-electrode and -layer approximate solution [11]. After an outline of the parameter fitting, we discuss the experimental measurements at the three depth settings as well as the fitted dielectric parameters. Finally, we suggest extensions that seek to resolve the skin layers in more detail and end with conclusions.

Materials and methods

Experiments

The experimental EIS measurements are from a previous study, which was carried out after ethics approval and informed consent [9].

In short, the study comprised 26 healthy, non-smoking subjects aged 27±6 (mean ± standard deviation) with an equal distribution of men and women without any known skin diseases or allergies; on the day of the measurements, they were asked to abstain from applying moisturizers. Before taking the EIS measurements with an in-house impedance spectrometer, SciBase I, the subjects' skin were stripped eighty times with Scotch® Magic™ Cellulose Tape on the volar forearm and then soaked with a physiological saline solution (at 0.9% salt concentration by mass) for 1 minute. Among the 26 measurements, two outliers were identified and excluded from further analysis: Their measured impedances were 15 kΩ and 50 kΩ at 1 kHz with no signs of double dispersion.

The circular noninvasive EIS probe—two voltage injection electrodes, a current detector and a guard ring—allows for 2-point measurements between 1 kHz and 1 MHz at 31 frequencies logarithmically distributed for five different current penetration depth settings, which arise from varying the applied voltage at the second injection electrode from 5 to 50 mV. As mentioned in the *Introduction*, in our earlier studies [6,9], only the depth setting 5 was employed; here, we use three depth settings: 1, 3 and 5.

Skin Thickness

For the mathematical model, we need the thickness of living epidermis as well as dermis for young subjects on the volar forearm. We calculated these in terms of weighted means and pooled standard deviations from a literature review summarized in Table 1, assuming that all data sets are normal-distributed:

$$\overline{X} = \frac{\sum_{i=1}^{m} X_i n_i}{\sum_{i=1}^{m} n_i}, \sigma_p = \left(\frac{\sum_{i=1}^{m} \sigma_i^2 (n_i - 1)}{\sum_{i=1}^{m} (n_i - 1)} \right)^{\frac{1}{2}}. \quad (1)$$

Here, $\overline{X}$ is the weighted mean, X_i is the mean in study i, n_i is the number of subjects in study i, m is the total number of studies, σ_i is the standard deviation of study i, σ_p is the pooled standard deviation.

First, we estimated the thickness of epidermis (ED) as 75±9 µm and the thickness of stratum corneum as 14±4 µm. By subtracting the mean thickness of stratum corneum from the thickness of epidermis and pooling their standard deviations, we found an estimate for the living epidermis thickness as 61±7 µm. Finally, we quantified the thickness of dermis as 1.0±0.2 mm.

Note that we combined the measurements from both males and females since we found no significant differences between them.

ED (μm)	Subj	Age	Measurement	Source
73.54±2.84	10	23 - 47	CM	[12]
89±9	15	19 - 24	CLSM	[13]
71.8±10	30	21 - 35	OCT	[14]
102±7.4	5	20 - 35	OCT	[15]
66.39±5.82	19	20 - 29	OCT	[16]
65.1±8.9	8	31 - 37	OCT	[17]
SC (μm)				
12.9±3.8	6	25 - 31	TEWL/Stripping	[18]
12.3±3.6	6	33.2±3.1	TEWL/Stripping	[19]
9.58±0.8	10	23 - 47	Reflectance CM	[12]
10.4±3.2	13	18 - 25	CLSM	[20]
22.6±4.33	14	23 - 49	CRS	[21]
18±3.9	14	28 - 50	CRS	[22]
10.4±0.9	9	23 - 55	OCT	[22]
13.07±2.12	19	20 - 29	OCT	[16]
18±2	2	23 - 25	CRS	[23]
DE (mm)				
1.02±0.10	44	21 - 30	US 20MHz B scanner	[24]
1.00±0.13	20	15 - 76	US 20MHz B scanner	[25]
1.02±0.21	17	16 - 50	Biopsy	[26]
0.85±0.11	5	26 - 74	US 22 MHz B scanner	[27]

Tab. 1: Skin thickness (mean value ± standard deviation) at the volar forearm for epidermis, stratum corneum and dermis. Some measurement techniques are: Confocal Microscopy (CM), Confocal laser scanning microscopy (CLSM), Optical coherence tomography (OCT), Transepidermal water loss (TEWL), Confocal Raman spectrometer (CRS) and Ultrasound (US).

Mathematical Model

We consider conservation of charge—ohmic and displacement currents—in the electrodes of the EIS probe and two layers—living epidermis and dermis—in the stripped skin as illustrated schematically in Fig. 1b and summarized in Appendix A. We further employ scaling arguments [10] to reduce the living epidermis and electrodes to boundary conditions, as illustrated in Fig. 1c, which yields a reduced model, outlined in Appendix B. The reduced model is then solved with a Hankel transform (see Appendix C), resulting in the following approximate analytical solution for the predicted impedance, Z_l, for a given depth setting l:

$$\begin{aligned} Z_l = (&A_{33}A_{41}A_{12} - A_{33}A_{41}A_{22} - A_{13}A_{21}A_{42} + A_{31}A_{13}A_{42} - \\ &A_{31}A_{13}A_{22} - A_{23}A_{41}A_{12} - A_{31}A_{23}A_{42} - A_{33}A_{12}A_{21} + \\ &A_{32}A_{41}A_{23} - A_{32}A_{41}A_{13} + A_{12}A_{21}A_{43} + A_{31}A_{12}A_{23} - \\ &A_{31}A_{12}A_{43} + A_{31}A_{22}A_{43} + A_{22}A_{41}A_{13} + A_{33}A_{42}A_{21} + \\ &A_{11}A_{33}A_{22} + A_{11}A_{32}A_{43} - A_{11}A_{33}A_{42} + A_{32}A_{13}A_{21} - \\ &A_{32}A_{43}A_{21} - A_{11}A_{22}A_{43} + A_{11}A_{23}A_{42} - A_{11}A_{32}A_{23}) / \\ &(-A_{12}A_{43}\alpha + A_{13}A_{22} - A_{32}A_{13} - A_{12}A_{23} + \\ &A_{33}A_{12} + A_{12}A_{23}\alpha + A_{43}\alpha A_{22} - A_{23}\alpha A_{42} - \\ &A_{13}\alpha A_{22} + A_{13}\alpha A_{42} - A_{33}A_{22} + A_{32}A_{23}), \end{aligned} \quad (2)$$

where

$$\mathbf{A} = \begin{bmatrix} -\frac{1}{SA_1} - \frac{2\pi I_{11}}{\sigma_{eff}^{DE}} & -\frac{2\pi I_{12}}{\sigma_{eff}^{DE}} & -\frac{2\pi I_{13}}{\sigma_{eff}^{DE}} & 1 \\ -\frac{2\pi I_{21}}{\sigma_{eff}^{DE}} & -\frac{1}{SA_2} - \frac{2\pi I_{22}}{\sigma_{eff}^{DE}} & -\frac{2\pi I_{23}}{\sigma_{eff}^{DE}} & 1 \\ -\frac{2\pi I_{31}}{\sigma_{eff}^{DE}} & -\frac{2\pi I_{32}}{\sigma_{eff}^{DE}} & -\frac{1}{SA_3} - \frac{2\pi I_{33}}{\sigma_{eff}^{DE}} & 1 \\ \frac{1}{SA_4} - \frac{2\pi I_{41}}{\sigma_{eff}^{DE}} & \frac{1}{SA_4} - \frac{2\pi I_{42}}{\sigma_{eff}^{DE}} & \frac{1}{SA_4} - \frac{2\pi I_{43}}{\sigma_{eff}^{DE}} & 1 \end{bmatrix}, \quad (3)$$

with

$$I_{ij} = \int_0^\infty \frac{(\kappa_j - \kappa_4)\kappa_i}{\tanh(\xi h_{DE})} d\xi, \quad (4)$$

$$\kappa_j(\xi) = \frac{R_{2j-1}J_1(R_{2j-1}\xi) - R_{2j-2}J_1(R_{2j-2}\xi)}{\pi\left(R_{2j-1}^2 - R_{2j-2}^2\right)\xi}, \quad (5)$$

where A_{ij} refers to the the i-th row and j-th column of the 4×4 matrix $\mathbf{A}$, I_{ij} is an integral from the Hankel transform, $J_1()$ refers to Bessel function of the first kind.

The parameters for the model are summarized in Table 2.

Current detection width, w_1	1 mm
Ceramic width, w_2, w_4, w_6	0.15, 0.15, 1.9 mm
Guard width, w_3	0.3 mm
Secondary inject width, w_5	0.5 mm
Primary inject width, w_7	0.5 mm
Living epidermis thickness, h_{LE}	61 μm
Dermis thickness, h_{DE}	1.0 mm
Inject voltage, V_0	0.05 V
Depth setting, α	0.1, 0.58, 1
Electrical permittivity in vacuum, ε_0 [28]	8.85 x10^{-12} Fm^{-1}

Tab. 2: Dimensions and material parameters.

Parameter Fitting

We employed the genetic optimization algorithm in Matlab [29] together with the measured and predicted impedance from Eq. 2 to fit the relative permittivity and resistance of the living epidermis and dermis throughout the frequency interval of 1 kHz to 1 MHz. The optimization was carried out by minimizing the objective function, $f(Z_1, Z_5, Z_1^{\exp}, Z_5^{\exp})$, defined as

$$f(Z_1, Z_5, Z_1^{\exp}, Z_5^{\exp}) = \left|\frac{\mathrm{Re}(Z_1)-\mathrm{Re}(Z_1^{\exp})}{\mathrm{Re}(Z_1^{\exp})}\right| + \left|\frac{\mathrm{Im}(Z_1)-\mathrm{Im}(Z_1^{\exp})}{\mathrm{Im}(Z_1^{\exp})}\right| + \left|\frac{\mathrm{Re}(Z_5)-\mathrm{Re}(Z_5^{\exp})}{\mathrm{Re}(Z_5^{\exp})}\right| + \left|\frac{\mathrm{Im}(Z_5)-\mathrm{Im}(Z_5^{\exp})}{\mathrm{Im}(Z_5^{\exp})}\right|, \quad (6)$$

for every subject and each measured frequency; i.e. a total of 744 times for our 24 subjects and 31 frequencies. Here, Re and Im denote the real and imaginary parts of the predicted impedance, Z_l, and measured counterpart, $Z_l^{\exp}$, at depth settings l=1 (α=1) and l=5 (α=0.1). In addition to the training set based on depth settings 1 and 5, a test set was taken from the middle depth, l=3 (α=0.58) for validation of the fitted dielectric properties. The depth settings 1 and 5 were chosen for the training set as they are the furthest apart in terms of the current injected; and the depth setting 3 was selected because it lies in between the two depths for training.

From a computational point of view, we note that the improper integrals, I_{ij}, only need to be solved numerically once before the fitting of the relative permittivity and resistivity, which is computationally efficient.

Ethical approval

The experimental EIS measurements were gathered under ethical approval and patient-informed consent.

Results and Discussion

Training set

The experimentally measured impedance—magnitude and phase in the frequency range from 1 kHz to 1 MHz—for the training set is shown in Fig. 2a,b. Here, the magnitude of the impedance is higher for depth setting 5, because less current is injected as compared to depth setting 1; similarly, the phase is less for depth setting 5. We also note that while the measured magnitude remains smooth and monotonically decreasing, the phase starts to fluctuate for frequencies around 100 kHz and higher.

According to a Lilliefors test at a significance level of 0.05 for each frequency, the magnitudes of depth setting 1 are all normal-distributed, whereas 71% of the magnitudes are normal-distributed for depth setting 5; similarly, 100% and 90% of the phases are normal-distributed for depth setting 1 and 5 respectively. We therefore assume that the measurements are normal-distributed.

In order to test that the means of the magnitude and phase of the impedance are not the same for depth 1 and 5, a paired *t*-Test at each of the 31 measured frequencies gives *P*-values, $P \lesssim 10^{-8}$. Even taking into account that we are carrying out multiple *t*-Tests and applying, e.g., a Bonferroni correction, we can state that the means are significantly different for our purposes. Here, we have employed a paired *t*-Test, because we paired two depths for each calibration of a given subject at each frequency. Likewise, a paired *t*-Test gives similarly small *P*-values ($P \lesssim 10^{-8}$ for $v \lesssim 10^5$ Hz) throughout the frequency range for the imaginary and real parts except around 1 MHz where the *P*-values for the imaginary parts become $O(10^{-1}$-$10^{-2})$.

Dielectric Properties

The means and standard deviations of the fitted resistivities and relative permittivities for the 24 subjects and 31 frequencies are depicted in Fig. 2c-d. The aforementioned measurement fluctuations only propagate to the fitted relative permittivity of the dermis above 100 kHz; the resistivities and relative permittivity of the living epidermis do not exhibit any significant fluctuations.

The mean dielectric properties for LE and DE can conveniently be written as exponential functions of fifth-order polynomials:

$$\rho^k(N) = 1[\Omega\mathrm{m}] \times 10^{(\mathrm{c}_5^k N^5 + \mathrm{c}_4^k N^4 + \mathrm{c}_3^k N^3 + \mathrm{c}_2^k N^2 + \mathrm{c}_1^k N + \mathrm{c}_0^k)}, \quad (7)$$

$$\varepsilon_r^k(N) = 10^{(\mathrm{d}_5^k N^5 + \mathrm{d}_4^k N^4 + \mathrm{d}_3^k N^3 + \mathrm{d}_2^k N^2 + \mathrm{d}_1^k N + \mathrm{d}_0^k)}, \quad (8)$$

$$N = \log_{10}(\tilde{\nu}) \quad (9)$$

Here, c_j^k and d_j^k are the material coefficients for the resistivity, ρ^k, and relative permittivity, ε^k, of the skin layers, given in Table 3; $\tilde{\nu} = \nu$ / (1 Hz) is a dimensionless frequency and N is the uppercase greek letter of ν, introduced for notational convenience; σ^k (= 1/ ρ^k), is the conductivity of layer *k*. These polynomials give overall smooth, monotonically decreasing dielectric properties without the fluctuations.

j	c_j^{LE}	d_j^{LE}
0	1.6306×10^{-2}	-2.3922×10^{-2}
1	-3.3591×10^{-1}	5.5919×10^{-1}
2	2.7019×10^{0}	-5.2033×10^{0}
3	-1.0667×10^{1}	2.4090×10^{1}
4	2.0531×10^{1}	-5.6056×10^{1}
5	-1.3260×10^{1}	5.7328×10^{1}

j	c_j^{DE}	d_j^{DE}
0	-1.0475×10^{-2}	-2.5399×10^{-1}
1	2.2902×10^{-1}	5.5554×10^{0}
2	-1.9609×10^{0}	-4.7903×10^{1}
3	8.2439×10^{0}	2.0330×10^{2}
4	-1.7209×10^{1}	-4.2527×10^{2}
5	1.4687×10^{1}	3.5741×10^{2}

Tab. 3: Coefficients for the conductivity and relative permittivity of the skin layers for 1 kHz to 1 MHz.

To the dielectric properties for living epidermis and dermis, we can add the polynomial counterparts from Birgersson [9] for the stratum corneum and adipose tissue for a complete four-layer description of the skin on the volar forearm from 1 kHz to 1 MHz.

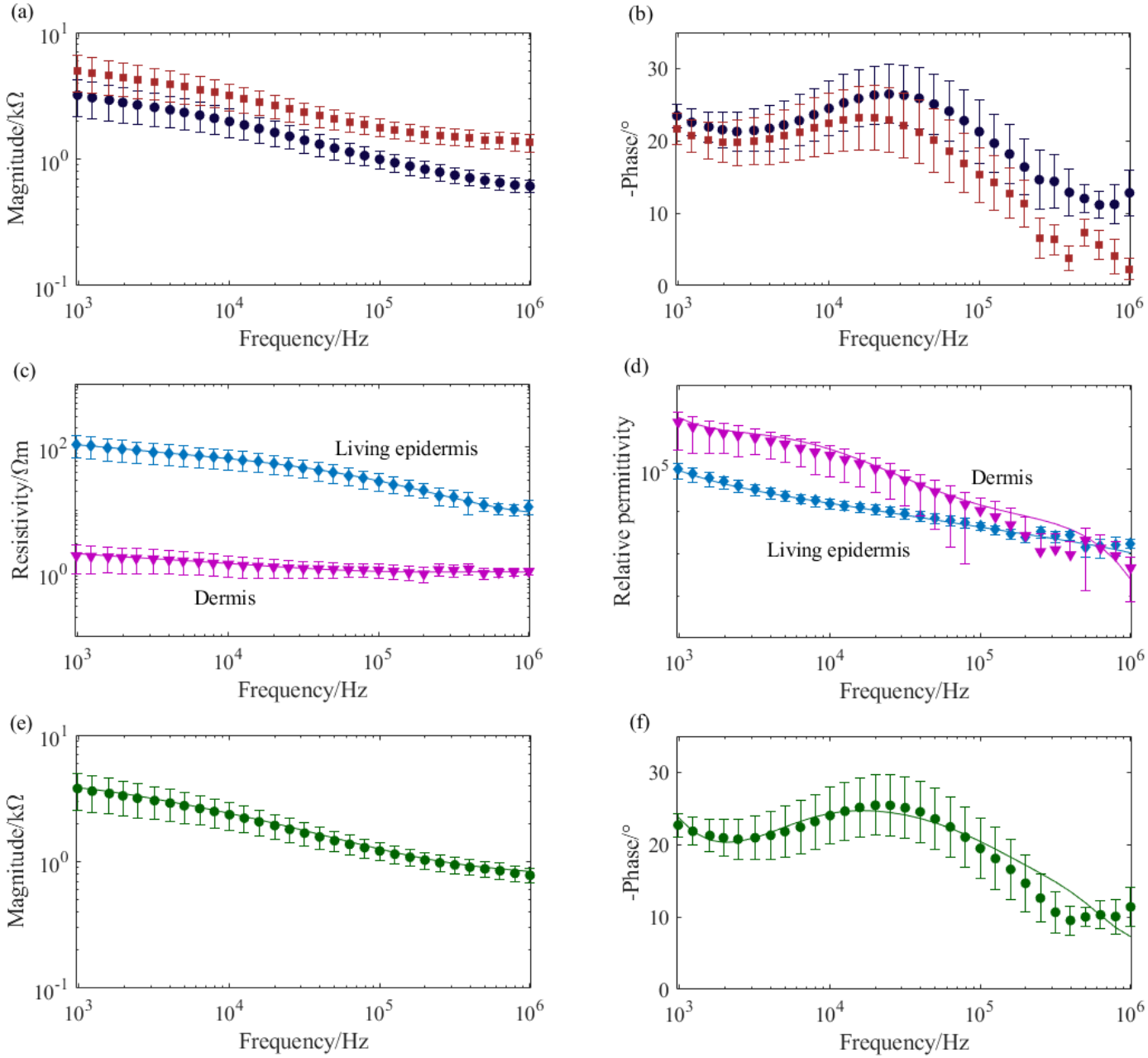

Fig. 2: The mean (depth 1 ●; depth 5 ■] and standard deviations (error bars) for the (a) magnitude and (b) phase of the experimentally measured impedances. The fitted mean resistivity and relative permittivity and their standard deviations can be found in (c) and (d) respectively for the living epidermis (♦) and dermis (▼); the fitted equations, Eqs. 7-8, are shown as lines. In (e) and (f), the validation set for depth setting 3 is shown for the experiments (●) and model predictions (lines).

Test set

The fitted functions for the dielectric properties were validated with the test set, as illustrated in Fig. 2e-f. We see that the test set displays the same behavior above around 100 kHz as the training sets for the measured phase. Most importantly, the model predictions agree well with the measured impedance at depth setting 3 throughout the frequency range except for the phase above 100 kHz; the phase does, however, stay within or almost within the standard deviations of the measurements.

According to a Lilliefors test at a significance level of 0.05 for each frequency, 100% and 93% of the magnitudes and phases of depth setting 3 are normal-distributed. We therefore take the measurements to be normal-distributed.

Taking paired *t*-Tests between depth 1 and 3 as well as depth 3 and 5 reveals $P \lesssim 10^{-5}$ throughout our frequency range, except around 1 MHz where the *P*-values for the phases become $O(10^{-2})$. Similarly, the paired *t*-Test gives similarly small *P*-values ($P \lesssim 10^{-4}$ for $\nu \lesssim 10^{5}$ Hz) throughout the frequency range for the imaginary and real parts, except again around 1 MHz where the *P*-values for the imaginary parts become $O(10^{-1}\text{-}10^{-2})$. Overall, we can consider the test set to be sufficiently different from the training set.

Resistivity

As expected, the mean resistivity is higher for the living epidermis than dermis (Fig. 2c): At 1 kHz, the mean LE resistivity is 110 Ωm whilst the mean DE resistivity is 1.9 Ωm; and at 1 MHz, the mean LE resistivity is 11 Ωm whilst the mean DE resistivity is 1.1 Ωm. Furthermore, the resistivity of the dermis does not vary as much as that of living epidermis.

Why did we expect this outcome? It is well known that a lower resistivity occurs when there is a larger number of mobile ions under the influence of an electric field [30]. In our case, there is a higher water content in the dermis than living epidermis [31], which contributes to a higher number of mobile ions in the presence of the applied electric field.

As an additional point of comparison for the dermis, we note that Tavernier [7] reported constant transversal and planar resistivities of around 0.6 Ωm and 0.4 Ωm respectively for in-vitro measurements between 1 kHz and 100 kHz. Now, while these values are lower than ours, mainly because they measured devitalized, fully saturated dermis tissue in a nutrient liquid rather than the in-vivo counterpart, which is influenced by the circadian rhythm and the persons' overall water content, their resistivities remain near-to constant as well.

Relative permittivity

The relative permittivity is a proportionality factor between the electric charge and the electric field, and reflects how much the bound charges can be displaced or polarized under the influence of an electric field [32]. From Fig. 2d, our measured in-vivo permittivity for the dermis decreases from around 10^6 to 10^2 in the frequency range from 1 kHz to 1 MHz, while that of the living epidermis is relatively constant on the order of 10^4. This frequency dependence of dielectric properties, known as β-dispersion, of the relative permittivity of dermis in the kHz frequency range occurs due to the polarization of cellular membranes, proteins and other organic macromolecules [33,34].

Returning to the measurements by Tavernier [7] for the dermis, we note that they found the relative permittivity to be around 10^6 (planar) and 4×10^5 (transverse) at 1 kHz, which is on the same order as ours; at 100 kHz, they found that the relative permittivity had dropped by around one order of magnitude, which is lower than our drop of around two orders of magnitude. Again, this is most likely due to the nature of their measurements.

Validation

We validate the model with the test case comprising the EIS measurement at a depth setting of 3, as illustrated in Fig. 2e-f. Overall, the predicted impedance based on the functions for the dielectric constants in the mathematical model agrees well with the measured counterpart in the frequency range for the magnitude and phase—although less so for the phase above 100 kHz. We attribute the increase in phase for depth settings 1 and 3 that appears after 100 kHz to noise in the measurements when the phase falls below around 10°, because we only expect the β-dispersion in this frequency range [34]. This is further supported by the fact that the mean phase for depth 5 does not suddenly increase at around 1 MHz and that the magnitudes of the impedance for the three depth settings are starting to even out around 1 MHz.

Referring back to the paired *t*-Tests to see whether the information we used for fitting based on depth settings 1 and 5 is sufficiently different from the training set, depth 3, we note that $P \lesssim 10^{-4}$ throughout most of the frequency range suggests that this is indeed the case. Overall, the validation should be sufficient for our purposes: viz., fitting of the dielectric properties of living epidermis and dermis. We could have split up the cohort into two subsets for the training and test sets instead of taking depth setting 3 for all subjects as the test set, but would not have been able to use all the available information for the fitting in doing so. Furthermore, depth setting 3 was selected because it gives a reasonably different magnitude, phase and pathway of the current in the stripped skin as compared to the other two depth settings—these are the physical phenomena that depend on the dielectric properties during EIS measurements of human skin.

Limitations

We have modeled a two-layer entity of stripped skin consisting of living epidermis and dermis by assuming homogenous and isotropic dielectric parameters. We have thus not captured any variations inside these two layers nor any anisotropic behavior. It might be possible to add at least the latter by also exploiting the experimental measurements at depth settings 2 and 4, which were not used in this study.

We did not model the subcutaneous layer, because we have shown through a current-distribution analysis [10] that the amount of current passing through the adipose tissue in the subcutaneous layer is negligible for our frequencies. Any current passing through the muscle tissue should therefore also be negligible.

We also did not consider additional factors such as the skin-electrode-interface impedance, hair follicles and sweat ducts since they are known to have a minor effect in the 1 kHz to 1 MHz frequency range with soaking [35-37].

From an experimental point-of-view, we note that there is scope to improve the measurements by fine-tuning the electrical-impedance spectrometer to be less sensitive to noise as we approach 1 MHz, which should result in smoother fitted dielectric properties even before fitting polynomials. Furthermore, one could increase the number of subjects as well as try to measure the stripping of stratum corneum.

Multi-scale extensions

The current mathematical model solves for a volume-averaged potential and total current that currently does not resolve the details of the cells or other structural features in the skin layers; therefore, the fitted dielectric parameters are also averages. In order to capture smaller-scale features, two extensions of the current work could be pursued.

The first extension would be to solve the three-dimensional transport of ohmic and displacement currents in a computational domain that comprises the relevant skin components—such as, e.g., cell membranes, cytoplasm and blood capillaries—numerically with the complex-valued PDE in a given skin layer whilst treating the other skin layers as averages to keep the computational cost reasonable and simulations tractable. We could then compare the simulated impedance with the experimental findings. This approach, however, would not lend itself easily to fitting of unknown dielectric parameters and their functional form with regards to the applied frequency due to the computational cost of geometrically resolving multiple length scales from the skin thickness down to the thickness of cell membranes, which brings us to the second extension.

In the second extension, we would apply the theory of volume-averaging [38] through a paper-and-pen approach to derive effective dielectric parameters for intrinsic potentials and superficial fluxes in the intra- and extracellular phases and the cell membranes that should result in a volume-averaged description that captures the leading order physics at multiple length scales yet is still computational cheap to solve. The key feature here is that multiple length scales will manifest themselves inside effective dielectric parameters and the interaction between the phases mathematically in the resulting PDE(s), and can therefore be solved in simple layers that we consider here. In fact, the set of equations we have solved in this paper represent one outcome from volume-averaging that lumps up all phases into one effective phase. Furthermore, this paper-and-pen analysis should allow us to write the dielectric properties not only as fifth-order polynomials but also as functions of parameters that describe the skin layer content, geometries and material properties: e.g., volume fractions of cells, dielectric properties of cell membranes, cytoplasm, and blood (depending on the skin layer). We have demonstrated both the suggested extensions in other engineering applications such as, e.g., organic [39,40] and perovskite [41] solar cells; and refer the interested reader to these for more ideas and a structured way to derive the volume-averaged equations for multi-scale systems that involve charge transport.

Conclusions

We have obtained new resistivity and permittivity values for the living epidermis and dermis of the human volar forearm, which are expressed as easy-to-use functions for frequencies between 1 kHz and 1 MHz; as well as weighted means and pooled standard deviations of epidermis, stratum corneum, living epidermis and dermis from a literature review. These thicknesses were employed in the mathematical model for conservation of charge that was fitted to the impedance measurements of stripped skin. In addition, we have discussed possible extensions to resolve more structural features of each skin layer.

Acknowledgements

The authors thank Ingrid Nicander for collecting the EIS data. The financial support from the National University of Singapore (NUS) is gratefully acknowledged.

Conflict of interest

Authors state no conflict of interest.

References

1. I. Nicander, M. Nyren, L. Emtestam, S. Ollmar, Baseline electrical impedance measurements at various skin sites related to age and sex, Skin Research and Technology 3 (4) (1997) 252-258. https://doi.org/10.1111/j.1600-0846.1997.tb00194.x
2. P. Åberg, U. Birgersson, P. Elsner, P. Mohr, S. Ollmar, Electrical impedance spectroscopy and the diagnostic accuracy for malignant melanoma, Experimental Dermatology 20 (8) (2011) 648-652. https://doi.org/10.1111/j.1600-0625.2011.01285.x
3. S. Gabriel, R. Lau, C. Gabriel, The dielectric properties of biological tissues: iii. parametric models for the dielectric spectrum of tissues, Physics in Medicine and Biology 41 (11) (1996) 2271. https://doi.org/10.1088/0031-9155/41/11/003
4. D. Miklavčič, N. Pavšelj, F. X. Hart, Electric properties of tissues, Wiley Encyclopedia of Biomedical Engineering. https://doi.org/10.1002/9780471740360.ebs0403
5. T. Yamamoto, Y. Yamamoto, Electrical properties of the epidermal stratum corneum, Medical and Biological Engineering 14 (2) (1976) 151-158. https://doi.org/10.1007/BF02478741
6. U. Birgersson, E. Birgersson, P. Åberg, I. Nicander, S. Ollmar, Non-invasive bioimpedance of intact skin: mathematical modeling and experiments, Physiological Measurement 32 (1) (2010) 1. https://doi.org/10.1088/0967-3334/32/1/001
7. A. Tavernier, M. Dierickx, M. Hinsenkamp, Tensors of dielectric permittivity and conductivity of in vitro human dermis and epidermis, Bioelectrochemistry and Bioenergetics 30 (1993) 65-72. https://doi.org/10.1016/0302-4598(93)80063-Z
8. A. Tavernier, M. Dierickx, M. Hinsenkamp, Conductivity and dielectric permittivity of dermis and epidermis in nutrient liquid saturation, in: Engineering in Medicine and Biology Society, 1992 14th Annual International Conference of the IEEE, Vol. 1, IEEE, 1992, pp. 274-275. https://doi.org/10.1109/IEMBS.1992.5760961
9. U. Birgersson, E. Birgersson, I. Nicander, S. Ollmar, A methodology for extracting the electrical properties of human

skin, Physiological Measurement 34 (6) (2013) 723. https://doi.org/10.1088/0967-3334/34/6/723

10. B. Tsai, H. Xue, E. Birgersson, S. Ollmar, U. Birgersson, Analysis of a mechanistic model for non-invasive bioimpedance of intact skin, Journal of Electrical Bioimpedance 8 (1) (2017) 84-96. http://dx.doi.org/10.5617/jeb.4826
11. B. Tsai, E. Birgersson, U. H. Birgersson, Mechanistic multilayer model for non-invasive bioimpedance of intact skin, Journal of electrical bioimpedance 9 (2018) 31-38. https://doi.org/10.2478/joeb-2018-0006
12. M. Huzaira, F. Rius, M. Rajadhyaksha, R. R. Anderson, S. González, Topographic variations in normal skin, as viewed by in vivo reflectance confocal microscopy, Journal of Investigative Dermatology 116 (6) (2001) 846-852. https://doi.org/10.1046/j.0022-202x.2001.01337.x
13. S. Neerken, G. W. Lucassen, M. A. Bisschop, E. Lenderink, T. A. Nuijs, Characterization of age-related effects in human skin: a comparative study that applies confocal laser scanning microscopy and optical coherence tomography, Journal of Biomedical Optics 9 (2) (2004) 274-281. https://doi.org/10.1117/1.1645795
14. T. Gambichler, R. Matip, G. Moussa, P. Altmeyer, K. Hoffmann, In vivo data of epidermal thickness evaluated by optical coherence tomography: effects of age, gender, skin type, and anatomic site, Journal of Dermatological Science 44 (3) (2006) 145-152. https://doi.org/10.1016/j.jdermsci.2006.09.008
15. G. Josse, J. George, D. Black, Automatic measurement of epidermal thickness from optical coherence tomography images using a new algorithm, Skin Research and Technology 17 (3) (2011) 314-319. https://doi.org/10.1111/j.1600-0846.2011.00499.x
16. T. Tsugita, T. Nishijima, T. Kitahara, Y. Takema, Positional differences and aging changes in Japanese woman epidermal thickness and corneous thickness determined by OCT (optical coherence tomography), Skin Research and Technology 19 (3) (2013) 242-250. https://doi.org/10.1111/srt.12021
17. C. Trojahn, G. Dobos, C. Richter, U. Blume-Peytavi, J. Kottner, Measuring skin aging using optical coherence tomography in vivo: a validation study, Journal of Biomedical Optics 20 (4) (2015) 045003. https://doi.org/10.1117/1.JBO.20.4.045003
18. K. A. Holbrook, G. F. Odland, Regional differences in the thickness (cell layers) of the human stratum corneum: an ultrastructural analysis, Journal of Investigative Dermatology 62 (4) (1974) 415-422. https://doi.org/10.1111/1523-1747.ep12701670
19. D. A. Schwindt, K. P.Wilhelm, H. I. Maibach, Water diffusion characteristics of human stratum corneum at different anatomical sites in vivo, Journal of Investigative Dermatology 111 (3) (1998) 385-389. https://doi.org/10.1046/j.1523-1747.1998.00321.x
20. K. Sauermann, S. Clemann, S. Jaspers, T. Gambichler, P. Altmeyer, K. Hoffmann, J. Ennen, Age related changes of human skin investigated with histometric measurements by confocal laser scanning microscopy in vivo, Skin Research and Technology 8 (1) (2002) 52-56. https://doi.org/10.1046/j.0909-752x.2001.10297.x
21. M. Egawa, T. Hirao, M. Takahashi, In vivo estimation of stratum corneum thickness from water concentration profiles obtained with raman spectroscopy, Acta Derm Venereol 87 (1) (2007) 4-8. https://doi.org/10.2340/00015555-0183
22. J. Crowther, A. Sieg, P. Blenkiron, C. Marcott, P. Matts, J. Kaczvinsky, A. Rawlings, Measuring the effects of topical moisturizers on changes in stratum corneum thickness, water gradients and hydration in vivo, British journal of Dermatology 159 (3) (2008) 567-577. https://doi.org/10.1111/j.1365-2133.2008.08703.x
23. L. Binder, S. SheikhRezaei, A. Baierl, L. Gruber, M. Wolzt, C. Valenta, Confocal raman spectroscopy: In vivo measurement of physiological skin parameters: a pilot study, Journal of Dermatological Science 88 (3) (2017) 280-288. https://doi.org/10.1016/j.jdermsci.2017.08.002
24. C. Tan, B. Statham, R. Marks, P. Payne, Skin thickness measurement by pulsed ultrasound; its reproducibility, validation and variability, British Journal of Dermatology 106 (6) (1982) 657-667. https://doi.org/10.1111/j.1365-2133.1982.tb14702.x
25. K. Hoffmann, M. Stuücker, T. Dirschka, S. Goörtz, S. El-Gammal, K. Dirting, A. Hoffmann, P. Altmeyer, Twenty MHz B-scan sonography for visualization and skin thickness measurement of human skin, Journal of the European Academy of Dermatology and Venereology 3 (3) (1994) 302-313. https://doi.org/10.1111/j.1468-3083.1994.tb00367.x
26. Y. Lee, K. Hwang, Skin thickness of Korean adults, Surgical and radiologic anatomy 24 (3-4) (2002) 183-189. http://dx.doi.org/10.1007/s00276-002-0034-5
27. Moore, M. Lunt, B. McManus, M. Anderson, A. Herrick, Seventeen-point dermal ultrasound scoring system - a reliable measure of skin thickness in patients with systemic sclerosis, Rheumatology 42 (12) (2003) 1559-1563. https://doi.org/10.1093/rheumatology/keg435
28. J. D. Jackson, Classical electrodynamics, Wiley, 1999, Ch. Appendix, pp. 780-781. http://as.wiley.com/WileyCDA/WileyTitle/productCd-047130932X.html
29. Matlab, Matlab r2018a (2018). URL www.mathworks.com/products/matlab
30. D. Dean, T. Ramanathan, D. Machado, R. Sundararajan, Electrical impedance spectroscopy study of biological tissues, Journal of Electrostatics 66 (3) (2008) 165-177. https://doi.org/10.1016/j.elstat.2007.11.005
31. K. Sasaki, K. Wake, S. Watanabe, Measurement of the dielectric properties of the epidermis and dermis at frequencies from 0.5 GHz to 110 GHz, Physics in Medicine & Biology 59 (16) (2014) 4739. https://doi.org/10.1088/0031-9155/59/16/4739
32. R. Pethig, D. B. Kell, The passive electrical properties of biological systems: their significance in physiology, biophysics and biotechnology, Physics in Medicine and Biology 32 (8) (1987) 933. https://doi.org/10.1088/0031-9155/32/8/001
33. H. P. Schwan, Electrical properties of tissue and cell suspensions., Advances in Biological and Medical Physics 5 (1957) 147. https://doi.org/10.1016/B978-1-4832-3111-2.50008-0

34. Ø. G. Martinsen, S. Grimnes, Bioimpedance and bioelectricity basics, Academic press, 2014, Ch. 3, p. 73. https://doi.org/10.1016/C2012-0-06951-7
35. Ø. G. Martinsen, S. Grimnes, Facts and myths about electrical measurement of stratum corneum hydration state, Dermatology 202 (2) (2001) 87-89. https://doi.org/10.1159/000051604
36. Ø. Martinsen, S. Grimnes, On using single frequency electrical measurements for skin hydration assessment, Innovation et Technologie en Biologie et Médecine 19 (1998) 395-400.
37. Ø. Martinsen, S. Grimnes, O. Sveen, Dielectric properties of some keratinised tissues. part 1: Stratum corneum and nail in situ, Medical and Biological Engineering and Computing 35 (3) (1997) 172-176. https://doi.org/10.1007/BF02530033
38. S. Whitaker, The method of volume averaging, Vol. 13, Springer Science & Business Media, 2013. https://doi.org/10.1007/978-94-017-3389-2
39. T. Zhang, E. Birgersson, J. Luther, A spatially smoothed device model for organic bulk heterojunction solar cells, Journal of Applied Physics 113 (17) (2013) 174505. https://doi.org/10.1063/1.4803542
40. T. Zhang, E. Birgersson, J. Luther, Modeling the structure-property relations in pillar-structured organic donor/acceptor solar cells, Organic Electronics 15 (11) (2014) 2742-2748. https://doi.org/10.1016/j.orgel.2014.07.036
41. H. Xue, R. Stangl, E. Birgersson, A spatially smoothed device model for meso-structured perovskite solar cells, Journal of Applied Physics, 124, 193103 (2018). https://doi.org/10.1063/1.5045379

Appendix A. Mathematical model

The full set of equations for the mechanistic model capturing charge transport can be expressed as follows (see [6] for a derivation of the model):

$$\Delta\Phi(r,z)=0, \tag{10}$$

$$\Phi(0\le r\le R_1, h_{LE}+h_{EL})=0, \tag{11}$$

$$\Phi(R_2\le r\le R_3, h_{LE}+h_{EL})=0, \tag{12}$$

$$\Phi(R_4\le r\le R_5, h_{LE}+h_{EL})=\alpha V_0, \tag{13}$$

$$\Phi(R_6\le r\le R_7, h_{LE}+h_{EL})=V_0, \tag{14}$$

with

$$\frac{\partial\Phi}{\partial n}=0, \tag{15}$$

for all the remaining boundaries; here, $\partial/\partial n$, is the normal derivative to a given boundary. The total current, **J**, in a skin layer, k (=LE, DE), is given by

$$J_r=-\sigma_{eff}^k\frac{\partial\Phi}{\partial r}, \tag{16}$$

$$J_\theta=0, \tag{17}$$

$$J_z=-\sigma_{eff}^k\frac{\partial\Phi}{\partial z}, \tag{18}$$

due to rotational symmetry. Here,

$$R_0=0, \tag{19}$$

$$R_j=R_{j-1}+w_j, \tag{20}$$

$$\sigma_{eff}^{DE}=\sigma^{DE}+i\omega\varepsilon_0\varepsilon_r^{DE}, \tag{21}$$

$$\sigma_{eff}^{LE}=\sigma^{LE}+i\omega\varepsilon_0\varepsilon_r^{LE}, \tag{22}$$

In the above equations, R_j are the radii that describe the EIS probe for j = 1, ..., 7; σ^k_{eff} is the effective, complex-valued electrical conductivity based on the conductivity, σ^k, and relative permittivity, ε_r^k, with the superscripts LE and DE denoting either living epidermis or dermis respectively; h is the thickness of a given layer, w is the width of a given layer or electrode, ε_0, is the relative permittivity of vacuum, ω is the angular frequency, V_0 is the applied voltage at the first inject, α is a factor that controls the voltage at the second inject, and i is the imaginary number.

Appendix B. Reduced model

The reduced model can be written as

$$\Delta\Phi(r,z)=0, \tag{23}$$

$$\frac{\partial\Phi(r,-h_{DE})}{\partial z}=0, \tag{24}$$

$$\frac{\partial\Phi(0,z)}{\partial r}=0, \tag{25}$$

$$\lim_{r\to\infty}\Phi(r,z)=0, \tag{26}$$

$$-\sigma_{eff}^{DE}\frac{\partial\Phi(r,0)}{\partial z}=\sum_{j=1}^{4}\Psi_j \tag{27}$$

where

$$\Psi_1=S\Phi(r,0)U(R_1-r)=\frac{I_1}{A_1}, \tag{28}$$

$$\Psi_2=S\Phi(r,0)\left[U(R_3-r)-U(R_2-r)\right]=\frac{I_2}{A_2}, \tag{29}$$

$$\Psi_3=S\left[\Phi(r,0)-\alpha V_0\right]\left[U(R_5-r)-U(R_4-r)\right]=\frac{I_3}{A_3}, \tag{30}$$

$$\Psi_4=S\left[\Phi(r,0)-V_0\right]\left[U(R_7-r)-U(R_6-r)\right]=\frac{I_4}{A_4}. \tag{31}$$

Here,

$$S=\frac{\sigma_{eff}^{LE}}{h_{LE}}, \tag{32}$$

$$A_j=\pi(R_{2j-1}^2-R_{2j-2}^2). \tag{33}$$

In the equations above, $U()$ denotes the Heaviside function, and A_j is the area at the j-th electrode (a total of four electrodes, as illustrated in Fig. 1). (See [10] for more details on the model reduction of a thin layer.)

Appendix C. Approximate analytical solution

The system of equations in Appendix B are here solved with a Hankel transform for a four-electrode probe. The Hankel transform of zeroth order, $\mathrm{H}_0\{\Phi(r,z)\}$,

$$\Psi(\xi,z)=\mathrm{H}_0\{\Phi(r,z)\}=\int_0^\infty r\Phi(r,z)J_0(\xi r)dr, \tag{34}$$

is first applied to Eq. 23 to obtain

$$\mathrm{H}_0\{\Delta\Phi(r,z)\}=-\xi^2\Psi(\xi,z)+\frac{\partial^2}{\partial z^2}\Psi(\xi,z)=0, \tag{35}$$

with the solution

$$\Psi(\xi,z)=A(\xi)e^{-\xi z}+B(\xi)e^{\xi z}, \tag{36}$$

where $A(\xi)$ and $B(\xi)$ are two functions that can be determined from boundary condition Eqs. 24 and 27 after their respective Hankel transforms as

$$A(\xi)=B(\xi)e^{-2\xi h_{DE}}, \tag{37}$$

$$B(\xi)=\frac{\sum_{j=1}^{4} I_j\kappa_j}{\sigma_{eff}^{DE}\xi(e^{-2\xi h_{DE}}-1)}. \tag{38}$$

Here, κ_j is defined in Eq. 4. With $A(\xi)$ and $B(\xi)$ in Eq. 36,

$$\Psi(\xi,z)=\frac{\sum_{j=1}^{4} I_j\kappa_j}{\sigma_{eff}^{DE}\xi(e^{-2\xi h_{DE}}-1)}(e^{-\xi(2h_{DE}+z)}+e^{\xi z}). \tag{39}$$

After taking the inverse Hankel transform, the average potential underneath the j-th electrode can be expressed as

$$\Phi_j^{avg}=\frac{2\pi}{A_j}\int_{R_{2j-2}}^{R_{2j-1}} r\int_0^\infty \xi\Psi(r,0)J_0(\xi r)d\xi dr+c=V_j, \tag{40}$$

where V_j is the prescribed potential at the j-th electrode from Eqs. 2-5 and c is the correction of the potential distribution arising from the Hankel transform. Since

$$I_4=-I_1-I_2-I_3, \tag{41}$$

and introducing this expression for I_4 into Eq. 40, yields the following system of linear equations:

$$\mathbf{A}\begin{bmatrix} I_1 \\ I_2 \\ I_3 \\ c \end{bmatrix}=\begin{bmatrix} 0 \\ 0 \\ \alpha V_0 \\ V_0 \end{bmatrix}, \tag{42}$$

where $\mathbf{A}$ is a matrix defined in Eq. 3. Once this linear system of equations is solved, the predicted impedance can be evaluated as

$$Z_l=\frac{V_0}{I_1}. \tag{43}$$